

# Submillimetre and near-infrared observations of galaxies selected at 170 $\mu\text{m}$

A. Sajina,<sup>1\*</sup> C. Borys,<sup>2</sup> S. Chapman,<sup>2</sup> H. Dole,<sup>3</sup> M. Halpern,<sup>1</sup> G. Lagache,<sup>4</sup>  
J.-L. Puget<sup>4</sup> and D. Scott<sup>1</sup>

<sup>1</sup>*Department of Physics & Astronomy, University of British Columbia, 6224 Agricultural Road, Vancouver, BC V6T1Z1, Canada*

<sup>2</sup>*Department of Physics, California Institute of Technology, Pasadena, CA 91125, USA*

<sup>3</sup>*Steward Observatory, University of Arizona, 933 N Cherry Ave, Tucson, AZ 85721, USA*

<sup>4</sup>*Institut d'Astrophysique Spatiale, Université Paris Sud, Bat. 121, 91405 Orsay Cedex, France*

Accepted 2003 May 12. Received 2003 April 29; in original form 2003 January 28

## ABSTRACT

We present results from James Clerk Maxwell Telescope (JCMT) submillimetre (submm) observations of sources selected from the *Infrared Space Observatory* (ISO) FIRBACK (Far-infrared Background) survey, along with United Kingdom Infrared Telescope (UKIRT) near-infrared imaging of a subsample. This gives valuable insight into the brightest  $\sim 10$  per cent of galaxies that contribute to the cosmic infrared background (CIB). We estimate the photometric redshifts and luminosities of these sources by fitting their spectral energy distributions (SEDs). The data appear to show a bimodal galaxy distribution, with normal star-forming galaxies at  $z \simeq 0$ , and a much more luminous population at  $z \sim 0.4\text{--}0.9$ . These are similar to the ultraluminous infrared galaxies which are found to evolve rapidly with redshift in other surveys. The detectability threshold of FIRBACK biases the sample away from much higher redshift ( $z \simeq 1.5$ ) objects. Nevertheless, the handful of  $z \sim 0.5$  sources that we identify are likely to be the low- $z$  counterparts of the typically higher- $z$  sources found in blank field submm observations. This subsample, being much more nearby than the average Submillimetre Common User Bolometer Array (SCUBA) galaxies, has the virtue of being relatively easy to study in the optical. Hence their detailed investigation could help elucidate the nature of the submm bright galaxies.

**Key words:** infrared: galaxies – submillimetre.

## 1 INTRODUCTION

What makes up the cosmic infrared background (CIB) detected from the *Cosmic Background Explorer* Far Infrared Absolute Spectrophotometer (COBE-FIRAS) data? (Puget et al. 1996; Dwek et al. 1998; Fixsen et al. 1998; Hauser et al. 1998; Lagache et al. 1999; Finkbeiner, Davis & Schlegel 2000; Lagache et al. 2000) This remains an open question, and details of galaxy types, their redshift distribution and how they appear in other wavebands remain sketchy. The FIRBACK (Far-infrared Background) survey (Puget et al. 1999; Dole et al. 2001) addressed this question by performing some of the deepest blank-field *Infrared Space Observatory* (ISO) surveys at 170  $\mu\text{m}$ , near the peak of that radiation. About 200 sources were detected above  $3\sigma$  ( $=135$  mJy), accounting for about 7 per cent of the nominal background value.

In general, far-infrared sources such as the FIRBACK ones sample the low-to-moderate redshift regime, and thus provide a link between

the local Universe and high- $z$  sources, such as the SCUBA<sup>1</sup>-bright ‘blank-sky’ population (see Blain et al. 2002, for a review). Understanding the nature of these sources, their emission mechanisms and their dust properties is crucial to our understanding of galaxy formation and evolution from high redshift until today. This in turn informs us about the cosmic background, as well as the nuclear activities, star formation distributions and the role of dust obscuration in star formation through a large fraction of the history of the Universe.

In order to understand the sources detected by FIRBACK better, we have been carrying out follow-up observations with SCUBA at 450 m and 850  $\mu\text{m}$ . Detection by ISO at 170  $\mu\text{m}$  ( $S_{170} > 135$  mJy) means that a strong bias away from high- $z$  objects is present, although we expect to detect objects out to  $z \simeq 1$  still. The FIRBACK galaxies represent the brightest contributors to the CIB, and are a different selection from typical SCUBA galaxies. ‘Blank-sky’ submillimetre (submm) bright galaxies, although accounting for up to 50 per cent of the submm background so far (e.g. Cowie, Barger &

\*E-mail: sajina@astro.ubc.ca

<sup>1</sup> Submillimetre Common User Bolometer Array.

**Table 1.** Multiwavelength data for our sample. All errors are  $1\sigma$  estimates.

Source	$K^a$ (mag)	$S_{100}^b$ (mJy)	$S_{170}^c$ (mJy)	$S_{450}^d$ (mJy)	$S_{850}^d$ (mJy)	$S_{1.4\text{GHz}}^e$ (mJy)
N1-001	12.4 ± 0.1	430 ± 87	597 ± 72	−3.0 ± 14.0	6.1 ± 1.6	0.74 ± 0.23
N1-002	12.7 ± 0.1	340 ± 121	544 ± 69	14.4 ± 12.4	4.4 ± 1.1	0.64 ± 0.04
N1-004	12.4 ± 0.0 <sup>†</sup>	300 ± 73	391 ± 58	32.5 ± 7.2	3.6 ± 1.4	0.88 ± 0.13
N1-007	13.2 ± 0.1 <sup>†</sup>	480 ± 73	338 ± 54	23.4 ± 8.1	4.4 ± 1.6	1.04 ± 0.12
N1-008	14.2 ± 0.1 <sup>†</sup>	160 ± 73	335 ± 54	25.9 ± 14.0	1.9 ± 1.1	2.98 ± 0.04
N1-009	12.0 ± 0.0	310 ± 58	313 ± 52	10.6 ± 7.6	3.5 ± 1.5	1.15 ± 0.11
N1-010	13.0 ± 0.0	360 ± 99	309 ± 52	15.2 ± 10.8	1.8 ± 1.4	1.05 ± 0.20
N1-012	13.9 ± 0.2	320 ± 122	302 ± 51	9.2 ± 10.0	1.5 ± 1.6	0.31 ± 0.07
N1-013	16.8 ± 0.1 <sup>†</sup>	350 ± 75	294 ± 51	18.8 ± 9.9	0.0 ± 1.5	0.52 ± 0.15
N1-015	14.8 ± 0.1	230 ± 41	294 ± 51	−3.4 ± 7.7	1.4 ± 1.6	0.52 ± 0.07
N1-016	13.2 ± 0.1	360 ± 92	289 ± 50	34.8 ± 16.7	1.5 ± 1.2	1.55 ± 0.13
N1-024	14.2 ± 0.0 <sup>†</sup>	<147	266 ± 49	32.3 ± 7.5	2.9 ± 1.3	0.75 ± 0.02
N1-029	14.3 ± 0.1	340 ± 83	229 ± 46	20.0 ± 14.2	0.5 ± 1.7	0.69 ± 0.05
N1-031	13.5 ± 0.1	110 ± 78	225 ± 46	9.2 ± 13.2	1.9 ± 1.1	0.43 ± 0.06
N1-032	18.5–19.5 <sup>†</sup>	220 ± 53	224 ± 46	14.9 ± 7.7	1.3 ± 1.4	0.21 ± 0.05
N1-034	19.3 ± 0.8 <sup>†</sup>	270 ± 71	221 ± 46	95.1 ± 27.5	1.3 ± 1.3	0.33 ± 0.07
N1-039	15.8 ± 0.2	230 ± 0	205 ± 44	10.9 ± 86.8	−0.1 ± 2.3	0.58 ± 0.07
N1-040	19.4 ± 0.6 <sup>†</sup>	<153	205 ± 44	29.2 ± 20.5	5.4 ± 1.1	0.33 ± 0.03
N1-041	14.7 ± 0.1	150 ± 55	204 ± 44	20.4 ± 156.7	−0.1 ± 2.5	0.76 ± 0.06
N1-045	14.4 ± 0.0 <sup>†</sup>	<165	198 ± 44	15.3 ± 8.3	3.0 ± 1.4	0.43 ± 0.06
N1-048	19.3 ± 0.9 <sup>†</sup>	<165	192 ± 44	15.5 ± 11.6	4.2 ± 1.1	0.37 ± 0.05
N1-056	15.9 ± 0.2	160 ± 71	179 ± 43	−8.6 ± 8.4	0.0 ± 1.6	0.24 ± 0.02
N1-059	20.4 ± 0.9 <sup>†</sup>	230 ± 66	175 ± 42	6.9 ± 34.5	6.4 ± 1.9	0.60 ± 0.06
N1-064	18.2 ± 0.3 <sup>†</sup>	260 ± 79	166 ± 42	35.2 ± 13.9	5.1 ± 1.2	0.23 ± 0.04
N1-068	15.3 ± 0.1 <sup>†</sup>	320 ± 95	165 ± 42	15.1 ± 7.6	2.2 ± 1.4	0.44 ± 0.05
N1-077	15.5 ± 0.2	200 ± 89	159 ± 41	5.9 ± 7.3	1.1 ± 1.3	0.40 ± 0.10
N1-078	18.0 ± 0.4 <sup>†</sup>	240 ± 63	158 ± 41	35.2 ± 8.7	5.7 ± 1.3	0.24 ± 0.04
N1-083	15.4 ± 0.2	< 195	150 ± 41	16.2 ± 16.0	0.7 ± 1.2	0.55 ± 0.03
N1-101	15.2 ± 0.2	210 ± 73	136 ± 40	19.8 ± 7.5	0.9 ± 1.5	0.39 ± 0.05
N1-153	15.5 ± 0.2	140 ± 58	103 ± 37	9.6 ± 15.3	−0.2 ± 1.0	0.24 ± 0.03
N2-013	–	310 ± 75	244 ± 53	23.5 ± 15.9	3.5 ± 1.4	0.30 ± 0.07

<sup>a</sup>These were obtained from our UKIRT sample (marked by <sup>†</sup>; see also Fig. 2) when available and from the 2MASS catalogue otherwise. Those fainter than  $K \sim 14$  were estimated directly from the 2MASS images.

<sup>b</sup>IRAS 100- $\mu\text{m}$  fluxes obtained using xscanpi (see text).

<sup>c</sup>ISOPHOT 170- $\mu\text{m}$  data from Dole et al. (2001).

<sup>d</sup>SCUBA 450- $\mu\text{m}$  and 850- $\mu\text{m}$  fluxes from this work.

<sup>e</sup>VLA 21-cm fluxes from Ciliegi et al. (1999).

Kneib 2002), make up an insignificant fraction of the total CIB. The combination of far-infrared and submm observations is thus very powerful in establishing a link between high- $z$  dusty starbursts and their local counterparts.

Observationally, without redshifts, it has been difficult to distinguish between cooler local starbursts and warmer, more luminous sources at higher  $z$ . This is because the spectral energy distributions (SEDs), for a fixed emissivity index  $\beta$ , are degenerate in the parameter combination  $(1+z)/T_d$ . There are additional complications, of course, caused by variations in  $\beta$ ,  $T_d$  and luminosity, changing the shape of the SED. Fundamentally, our understanding of dust in extragalactic sources, its properties and interaction with the radiation field is poor, which is a major impediment in our interpretation of the observational evidence.

The only way to approach these issues is by detailed multiwavelength studies of samples representing key elements in the above puzzle.

The data we present in this paper constitute a far-infrared selected sample. This sample is now large enough, and with wide enough wavelength coverage, including near-infrared, far-infrared,

submm and radio observations, to be able to tackle some of these issues. We do this through a combination of direct SED fitting, statistical analysis, consistency with other observations and comparison with model predictions, trying to use the minimum number of a priori assumptions. In essence, we start with the assumption that our sources represent a uniform population, which we demonstrate are most likely local star-forming galaxies. This model breaks down for a handful of our sources, which probably results from their being at somewhat higher redshifts (and more luminous) than the rest of the sample. Because our sample is representative of FIRBACK as a whole, we have thus improved our knowledge of the nature of the brightest sources making up the CIB.

We focus largely on the conclusions deriving from the submm observations. Discussion of the individual properties of FIRBACK galaxies in general, including issues relating to the identification of the sources, will be discussed elsewhere (Lagache et al., in preparation).

Throughout the paper, we assume a flat Universe with  $H_0 = 75 \text{ km s}^{-1} \text{ Mpc}^{-1}$ ,  $\Omega_M = 0.3$  and  $\Omega_\Lambda = 0.7$ .

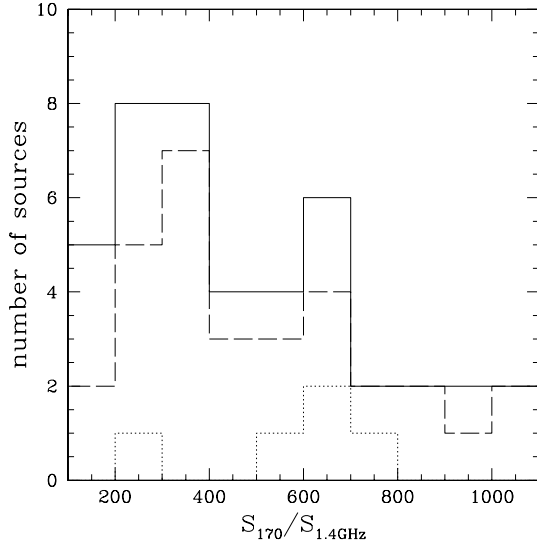


**Figure 1.** Distribution of the  $S_{170}/S_{1.4\text{GHz}}$  ratio. The solid histogram represents the 41 sources from the FIRBACK catalogue which meet our selection criteria. The dashed histogram is our subsample of 31 targets. The dotted line shows our high- $z$  candidates (discussed in Section 4).

## 2 THE DATA

### 2.1 Sample

Targets were selected from the FIRBACK ( $>3\sigma$ ) catalogue (Dole et al. 2001) in the ELAIS N1 field. Confusion remains a major issue with a beam size of  $\sim 90$  arcsec. In our selection, we aimed at a uniform sample that would be as representative of the FIRBACK population as possible. Our main selection criterion has been the availability of radio detections (Ciliegi et al. 1999) inside the beam [required for James Clerk Maxwell Telescope (JCMT) pointing].

We exclude FIRBACK sources with radio-bright counterparts which are rare and are not representative of the typical FIRBACK source, as well as sources with several radio detections per beam.<sup>2</sup> This left us with 41 possible sources to draw from – we have followed up 30 (and additionally one N2 source), listed in Table 1. Because of this broadness of selection criteria, we believe our sample represents a fair cross-section of the FIRBACK population, rather than focusing on a specific subpopulation. This can be seen clearly in Fig. 1, where there is close agreement between the distribution of  $S_{170}/S_{1.4\text{GHz}}$  for all 41 possible sources and the distribution of the 30 sources in our sample.

### 2.2 SCUBA submm observations

The observations presented here were taken with the SCUBA (Holland et al. 1999) instrument on the JCMT in 1999 March and in 2001 March and May. In order to avoid biasing our data, we attempted to observe each source until a predetermined rms ( $\sim 1.5$  mJy) was reached, irrespective of whether the source appeared to be a possible detection or not. The 2001 March data were taken in exceptional grade 1 weather ( $\tau_{225} \sim 0.04$ , and as low as 0.02), whereas the 1999 data were taken in merely ‘good’ weather ( $\tau_{225} \sim 0.07$ ). Throughout our observations, we used the two-bolometer chopping mode. This involves chopping in array coordinates in order

<sup>2</sup>This criterion was not applied too strictly: a few sources (N1-008, N1-029, N1-041) do, in fact, have two radio sources inside the beam.

to always align one negative beam exactly with a specific off-centre bolometer, with the other being partially aligned. Thus the negative beams can be folded in, improving the rms by a factor of up to  $\sqrt{2/3}$ . Unfortunately, for our 2001 run, software problems with the new telescope control system resulted in SCUBA not properly chopping on to another bolometer, making the negative beams unrecoverable. Thus the 2001 data presented here are from the central bolometer only, whereas the 1999 data have the negative beams folded in.

The data were reduced using the SURF package (Jenness & Lightfoot 1998) and also with custom-written code. The extinction correction was performed using sky-dip observations whenever available, and with a derived optical depth from the  $\tau_{\text{CSO}} - \tau_{\text{SCUBA}}$  relations (where CSO is the Caltech Submillimeter Observatory) (Archibald, Wagg & Jenness 2000) otherwise. The sky was subtracted as a mean level for the entire array at each jiggle, excluding the signal bolometers as well as any bad bolometers, as revealed by excessive noise levels. A calibration uncertainty of a maximum of 20 per cent exists (based on differences among the nightly calibration values); however, it has little effect on the signal-to-noise ratios, especially for the 2001 data, where each source was typically observed in a single night. The pointing uncertainty was  $\sim 2$  arcsec. The SCUBA 850- $\mu\text{m}$  beam FWHM is  $\sim 15$  arcsec, whereas the 450- $\mu\text{m}$  beam FWHM is  $\sim 8$  arcsec.

The derived 450- and 850- $\mu\text{m}$  flux densities and associated  $1\sigma$  errors are listed in Table 1.

### 2.3 UKIRT near-infrared observations

Most of our SCUBA-detected FIRBACK sources could not be identified in Digital Palomar Sky Survey (DPOSS) images. As the sources are expected to be extinguished by dust and therefore have red spectra, we obtained deep observations in the  $K$ -band at the United Kingdom Infrared Telescope (UKIRT), using the Fast Track Imager (UFTI) for maximum sensitivity to obscured components. The small UFTI field ( $50 \times 50$  arcsec<sup>2</sup>) was centred on the source positions taken from the radio/SCUBA identifications. Each source was imaged for a total of 1800 s, with individual exposures of 60 s each, reaching a limiting magnitude in a 2-arcsec diameter aperture of  $K = 20.4$  ( $5\sigma$ ). The fast tip/tilt, adaptively corrected imaging resulted in seeing better than median conditions, at  $\simeq 0.4$  arcsec FWHM. Data were reduced using the Starlink UKIRT/UFTI image processing tools under the ORACDR environment (Bridger et al. 2000). We wrote custom ORACDR scripts to optimize point-source sensitivity in our essentially blank field observations, creating flat fields from each 9-point dither, and high signal-to-noise thermal background images from 60 min of data centred around the observing period of each target. Fig. 2 shows the available UKIRT images. For the rest of our sample, we use data from the Two Micron All Sky Survey (2MASS) catalogue (for sources with  $K \sim 14$ –15, we estimated their magnitudes directly from the calibrated catalogue images via aperture photometry in GAIA).

### 2.4 Far-infrared and radio fluxes

*IRAS* 100- $\mu\text{m}$  fluxes were obtained using the XSCANPI facility. We quote them here for the sake of completeness, as well as to help in comparison with local *IRAS* galaxies (which are typically  $> 1$  Jy). The errors quoted are purely statistical; however, at this faint level systematic errors (including, among other things, infrared cirrus and mapping artefacts) dominate the flux estimates, to the point of making them of little statistical use. *ISO* Photometer (ISOPHOT) 90- $\mu\text{m}$  detections also exist for a few of the objects, as well as

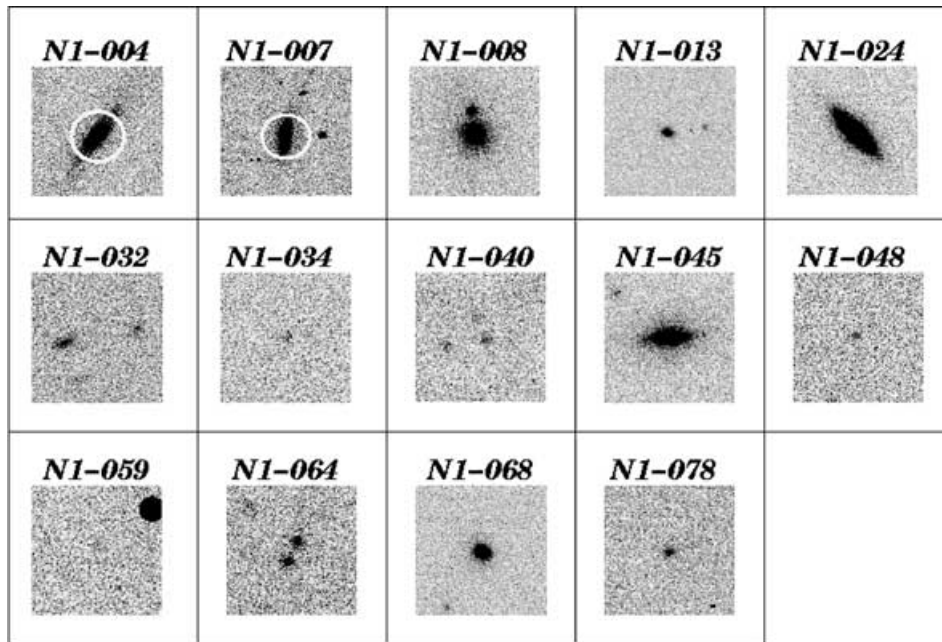


**Figure 2.** The available UKIRT *K*-band images. The images are centred on the radio position, and are about  $15 \times 15 \text{ arcsec}^2$  or roughly a SCUBA  $850\text{-}\mu\text{m}$  beam size. Exceptions are N1-004 and N1-007, where the white circles have a diameter of  $\sim 15 \text{ arcsec}$ .

mid-infrared *ISO* Camera (ISOCAM) data. We do not use these data as they are too sparse (typically  $< 5$  sources) and provide little constraint on the thermal far-infrared/submm, which is our main focus here.

The radio fluxes at 1.4 GHz given in Table 1 are from a Very Large Array (VLA) survey of the field (Cilieggi et al. 1999), and errors are  $1\sigma$ .

### 3 RESULTS AND ANALYSIS

#### 3.1 Assembling the multiwavelength data

The 1999 data presented here were previously discussed in Scott et al. (2000).<sup>3</sup> However, we re-reduced the old data concurrently with the 2001 data in order to ensure uniformity, especially as an up-graded version of SURF and a new custom-written code were used. We confirm all previously reported detections (i.e. targets having a signal-to-noise ratio of  $S/N > 3$ ). The 2001 data have three unambiguous detections at  $450 \mu\text{m}$  (N1-004, N1-024, N1-078). This high detection rate at a difficult band is a result of the exceptional atmospheric conditions during our observing run, as well as the far superior performance of the new wide-band filter. In addition, there are three new detections at  $850 \mu\text{m}$  (N1-001, N1-059, N-078). Note that the few-arcsecond pointing uncertainty (see Section 2.2) has only a small effect on the long-wavelength data, but may be a significant reason for the apparently missing  $450\text{-}\mu\text{m}$  flux (where the beam FWHM is only  $\sim 8 \text{ arcsec}$ ) in sources where one would expect to find some (e.g. N1-059). Our results for the entire sample are presented in Table 1, which, in addition to the submm data, includes near-infrared, far-infrared and radio data. The sample as a whole is strongly detected, with average fluxes of  $\langle S_{850} \rangle = 2.6 \pm$

$0.2 \text{ mJy}$  and  $\langle S_{450} \rangle = 16.7 \pm 1.9 \text{ mJy}$ . This is indicative of the fact that, although most sources do not clear the  $3\sigma$  detection threshold, there is useful statistical information in the flux data (far in excess of what would be expected for mere sky fluctuations). Thus we treat these fluxes directly, along with their uncertainties, rather than only using the upper limits. Here, we focus on the general properties of the sample which are revealed by the addition of the submm and near-infrared data. Physical properties for individual sources will be explored elsewhere (Lagache et al., in preparation).

Two possible sources of uncertainty in comparing the far-infrared and SCUBA fluxes are: (1) the different sizes of the *ISO* (about  $90 \text{ arcsec}$ ) and SCUBA (about  $15 \text{ arcsec}$ ) beams, and thus the possibility of multiple sources lying within the beam – this is also complicated by the issue of clustering, and possibly lensing; and (2) the relative proximity of the bulk of our sources, and thus the possibility of at least a few being extended beyond the SCUBA beam (see, for example, N1-004 and N1-007 in Fig. 2). This is especially severe for the  $\sim 8\text{-arcsec}$   $450\text{-}\mu\text{m}$  beam. In general, however, images at other wavelengths are insufficient to determine precisely how much flux is being lost in this way, as it is not clear how concentrated the submm emission would be, or how it is distributed in comparison with other wavebands. In any case, the submm flux estimates are likely to be less accurate in photometry mode if the source size is of the order of the beam size. These effects, of course, become more important with increasing  $S_{170}$ .

Although the low submm flux of most of our sources is consistent with local star-forming galaxies, there is the additional concern about the possibility of cirrus contamination of the FIRBACK sample. Previous studies have discussed this issue extensively (Lagache & Puget 2000; Puget et al. 1999), concluding that the FIRBACK sources are unlikely to suffer from significant cirrus contamination. The N1 field was chosen for this survey because of its low cirrus emission. We can estimate, using the standard formula (Helou & Beichman 1990), that the cirrus variance is  $\sim 10$  times less than the detection cut-off of the FIRBACK survey. Because of the

<sup>3</sup>Note that we use the naming scheme of Dole et al. (2001), which differs from the earlier convention used. In particular, N1-038, N1-061 and N1-063 from Scott et al. (2000) correspond to the new N1-040, N1-048 and N1-064.



non-Gaussianity of the cirrus fluctuations (Gautier et al. 1992), some outliers are still possible, but these would have to reside in very cold cores, which have not been revealed in deep searches for CO emission. Moreover, the far-infrared slope of cirrus knots is known to be much steeper than that of the sources. A study, whose source selection is similar to that of FIRBACK (Juvela, Mattila & Lemke 2000), makes use of this in concluding that cirrus contamination is highly unlikely. In agreement with that study, our sources show a fairly flat  $S_{100}/S_{170}$  ratio. Finally, all our FIRBACK sources have a radio counterpart, reducing the chance that cirrus contamination is relevant even more.

### 3.2 Linear correlations

Fig. 3 shows three illustrative projections for our data, using the 170-, 450-, 850- $\mu\text{m}$  and radio fluxes. For each plot, a fit is made to all points using a straight line passing through the origin, i.e.  $y = mx$ . Then the  $>2\sigma$  outliers are excluded, a new fit is made and is plotted along with the rms scatter. Table 2 shows the results. Because, in most cases, the errors in the two directions are of comparable size, rather than use the conventional 1D  $\chi^2$ , we minimize a statistic which combines errors in both directions:

$$\chi_{2D}^2 = \sum_{i=1}^N \frac{(y_i - mx_i)^2}{(\sigma_{y_i}^2 + m^2\sigma_{x_i}^2)}, \quad (1)$$

where  $\sigma_x$  and  $\sigma_y$  are the two errors. In general, it appears that the typical uncertainties of our submm data points are larger than the  $1\sigma$  scatter of the fits. We test this explicitly for the  $S_{450}$  versus  $S_{850}$  plot via Monte Carlo simulations of the data, thereby estimating the probability of the  $\chi_{2D}^2$  obtained to be  $\sim 2$  per cent. This implies that our errors are overestimated by a factor of  $\sim\sqrt{2}$ , or else there is some as yet unidentified source of correlation in the errors. We will, however, be conservative and leave the errors as they are, because we cannot account for the source of this discrepancy properly.

After this cautionary aside, we return to Fig. 3. It is organized such that the order roughly follows the main features of the long wavelength SED: the top plot tracks the location of the thermal peak largely; the middle plot corresponds to the submm slope; and the bottom plot traces the trough between the thermal and the non-thermal emission.

First, we will concentrate on the  $S_{850}$  versus  $S_{170}$  plot (Fig. 3a). We notice immediately that about five sources (the circled crosses) occupy a locus  $>2\sigma$  away from the best-fit line. Assuming a grey-body model, these sources are either at higher redshift or lower temperature than the rest of the FIRBACK 170- $\mu\text{m}$  sources (or a combination of both).

To understand which, we turn to the  $S_{450}$  versus  $S_{850}$  plot (Fig. 3b). Here, we are mainly exploring the slope of the spectrum in the submm. What we notice in this plot is that there is not a population of outliers as there was in the  $S_{850}$  versus  $S_{170}$  plot (the only outliers are N1-001, N1-034 and N1-059, which all have submm slopes which cannot be fit by any sensible dust/redshift combination alone, and thus we assume that they suffer from some systematic effect such as that discussed in Section 3.1). This common distribution implies that a single  $[\beta, T/(1+z)]$  combination describes the sample reasonably well. The lack of the outliers, from the  $S_{850}$  versus  $S_{170}$  plot (Fig. 3a), means that the (N1-040, N1-048, N1-064, N1-059, and N1-078) location of the five outliers in Fig. 3(a) is most likely owing to their having somewhat higher  $z$  rather than their having a significantly different SED shape. In addition, their redshifts can only be as high as  $z \sim 1$ , corresponding roughly to the shift between 170  $\mu\text{m}$  and

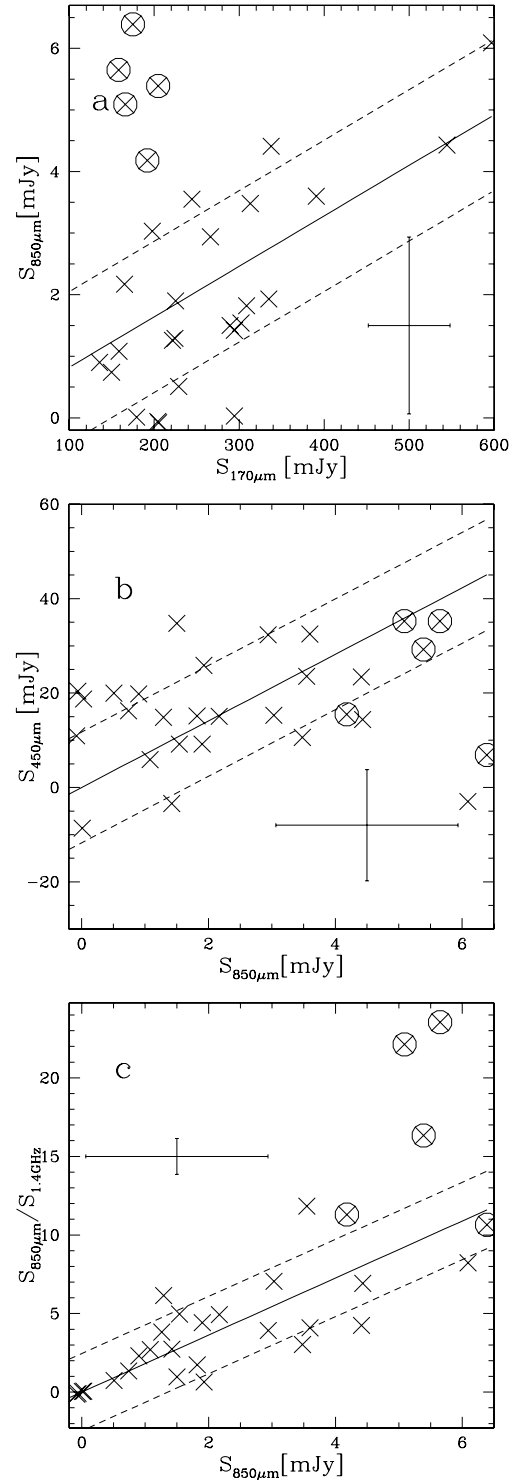


**Figure 3.** Multiwavelength projections of our data. The solid lines are the  $y = mx$  fits obtained by minimizing  $\chi_{2D}^2$  in equation (1). The dashed lines are the  $\pm 1\sigma$  scatter of the points around the lines, with the fit parameters given in Table 2. The error bars shown are representative for our data. The five outliers in panel (a) are indicated with the same symbols in the other two panels.

450  $\mu\text{m}$  (a higher-redshift, much warmer population would have to be very finely tuned to still fall on the same distribution, which seems improbable). This, in turn, constrains the temperature of the sources roughly (by Wien's law) to less than about 40 K.

**Table 2.** Results for the linear fits to the data.

Relation	m	rms	$\chi^2$
850 $\mu\text{m}$ versus 170 $\mu\text{m}$	0.01	1.23	18.07
450 $\mu\text{m}$ versus 850 $\mu\text{m}$	7.05	11.74	13.95
850 $\mu\text{m}/1.4$ GHz versus 850 $\mu\text{m}$	1.82	2.46	12.19

We now turn to Fig. 3(c), the 850  $\mu\text{m}/1.4$  GHz versus 850  $\mu\text{m}$  comparison, where the previous outliers return again [except for N1-059, which has unusually high radio emission, (discussed later)], confirming that redshift, rather than dust properties, is indeed the main difference between them and the rest of the sample.

### 3.3 Submm/radio redshifts

As a tracer of the trough between the thermal and the non-thermal emission of galaxies,  $S_{850}/S_{1.4\text{GHz}}$  is commonly used as a redshift indicator (Carilli & Yun 2000). It is, however, degenerate in dust properties for galaxies cooler than about 60 K (Blain et al. 2002). Because we are clearly in that regime (see previous section), we have investigated using this relation calibrated on samples with different selections. The first parametrization we used was the Carilli & Yun relation (Carilli & Yun 2000, CY hereafter) which is based on *IRAS*-selected and somewhat more radio-loud galaxies, with likely a higher fraction of active galactic nuclei (AGN). The second parametrization we used was that from Dunne, Clements & Eales (2000) (DCE hereafter), which is based on the SCUBA Local Universe Galaxy Survey (SLUGS) sample (Dunne & Eales 2001), which is essentially an *IRAS*-bright local selection (unlike ours).

In general, such relations provide too weak a constraint on individual redshifts locally, owing to the large scatter in intrinsic galaxy properties. However, they still confirm our prior selection of N1-040, N1-048, N1-064, N1-059 and N1-078 as likely being at somewhat higher redshifts than the rest of the galaxies in our sample (based on both relations giving a redshift of  $>0.4$  for all of these sources). The only other source which satisfies this is N2-013. We return to it in Section 3.6, when we also discuss different redshift estimators.

### 3.4 Submm versus near-infrared

Here, we examine the correlation between the  $K$  magnitudes and 850- $\mu\text{m}$  fluxes of our sources. The  $S_{850}$  flux density by itself is not a good redshift indicator because of its  $k$ -correction behaviour. It is, however, a good luminosity tracer. The  $K$  magnitude (in the rest frame) is also a luminosity indicator, as it is 10 times less obscured than the optical. The  $S_{850}$  to  $K$  magnitude relation can be used as a redshift indicator (Barger, Cowie & Sanders 1999; Dannerbauer et al. 2002) because the rest-frame shorter wavelengths (that are much more dust-obscured) move with increasing redshift into the observer-frame near-infrared. Thus the  $K$  magnitude for a given submm flux is dependent on both redshift and dust obscuration. Fig. 4 plots the flux at 850  $\mu\text{m}$  against  $K$  magnitude, where the higher- $z$  sources populate clearly a different locus from the nearby galaxies. They are roughly  $3\sigma$  removed from the best-fitting relation for the other sources, with a distinct gap between the two groups (apart from a couple of sources which we discuss later). The gap is more pronounced than in Fig. 3, as here the  $(1+z)/T_d$  degeneracy is somewhat broken.

A redshift relation based solely on the  $K$  magnitude is bound to be degenerate in some other galaxy properties (amount of dust,

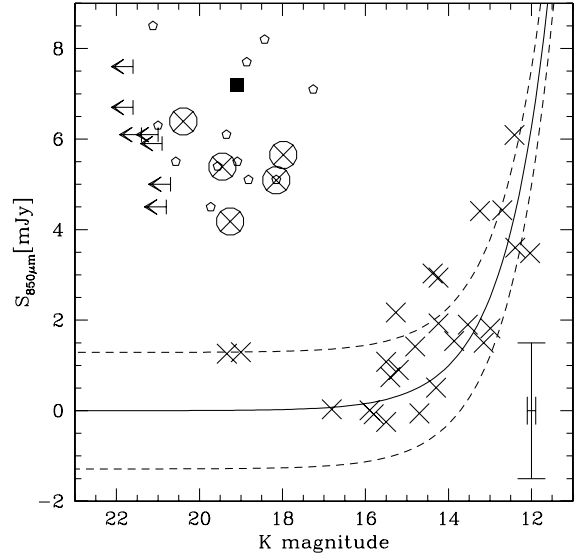


**Figure 4.**  $S_{850}$  versus  $K$  magnitude for our sample (crosses, with the five outliers also encircled). The filled square and  $K$ -band upper limits are from the SCUBA lens survey (Smail et al. 2002), with the pentagons being from the UK 8-mJy survey (Ivison et al. 2002). Our high- $z$  candidates populate a similar region to these other SCUBA survey sources. The solid line is a log-log fit to the crosses only, with the dashed lines being the  $\pm 1\sigma$  scatter. The error bar in the lower right-hand corner is a representative one for our measurements.

luminosity, etc.), and can work only for a very homogeneous sample of galaxies (see e.g. Willott et al. 2003). The addition of submm flux improves this relation, because the  $K$ -band is dust-absorption attenuated (specifically for distant, luminous galaxies), whereas the submm flux arises from dust emission, and thus the combination of the two will break the dust degeneracy somewhat. This diagnostic of both the absorption and emission spectrum allows for a more robust redshift indicator over different galaxy types. What is robustly clear is that, in general, objects which are detected at 850  $\mu\text{m}$  and are faint at  $K$ -band are at higher redshift. In Fig. 4, we find the same handful of outliers as in Sections 3.2 and 3.3.

### 3.5 SED fits

Now we fit single greybody SEDs to the 170-, 450- and 850- $\mu\text{m}$  fluxes of each source (see Fig. 5). We assume optically thin sources; the effect of including a non-negligible  $\tau$  in the fits is to suppress the peak with respect to the Rayleigh–Jeans tail, such that the best-fitting dust temperature inferred will be 10–20 per cent higher than otherwise (Blain et al. 2002). This is therefore not an important effect for submm spectra dominated by single-temperature dust emission (to the precision of our fits of three points). In order to avoid stretching these assumptions too much, we only use the 170-, 450- and 850- $\mu\text{m}$  fluxes in the fits, where the SED is dominated by the coldest significant dust component.

We fit for two parameters – the overall normalization, which gives the luminosity (if the redshift is known), and the wavelength shift, which is proportional to  $(1+z)/T_d$ . The best fit  $\chi^2$  and fit parameters were obtained with the PIKAIA genetic algorithm (Charbonneau 1995). With only three points for each galaxy, we could not also fit for the emissivity index  $\beta$ , and therefore it was held constant. However, we investigated how different values of  $\beta$  (1.3, 1.5, 1.7 and 1.9) would affect the quality of fits for the sample as a whole.

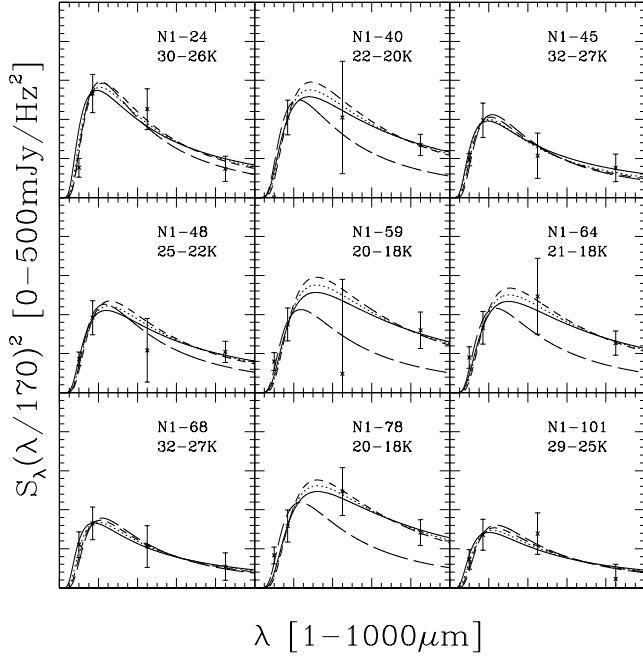


**Figure 5.** The SED fits for a fraction of our sample where the fits suggest a non-zero redshift. The axes scales are linear, with the  $x$ - and  $y$ -ranges in all panels being the same (shown in the labels); the sources are arranged by decreasing 170- $\mu\text{m}$  flux. The *IRAS* 100- $\mu\text{m}$  points included in the plots are not used in the fit. For the sake of clarity, we rescale the flux via  $(\lambda/170\mu\text{m})^2$ . This was necessary as there is typically an order of magnitude difference between the the far-infrared and submm fluxes, and in this way the submm – which is the focus of this work – is emphasized. The solid line corresponds to  $\beta = 1.3$ , the dotted line to  $\beta = 1.5$ , the short-dashed line to  $\beta = 1.7$  and the long-dashed line to  $\beta = 1.9$ . The truncated temperatures shown are in units of  $\frac{T}{(1+z)}$  and correspond to the  $\beta = 1.5$  and 1.7 cases, respectively. See the text for an explanation of this choice, as well as further discussion on the fits.

Values of  $\beta = 1.5$ – $1.7$  are far better than either smaller or larger values, for which a third of the sample has a  $\chi^2 > 2$ . The sources, with a poor fit in all cases, are N1-001, N1-002, N1-015, N1-034 and N1-056. For the lowest  $\beta$  tested, five additional sources show a poor fit: N1-008, N1-009, N1-012, N1-013 and N1-016 (note that these are all among the brighter *ISO* sources in our sample). On the other hand, the higher ( $\beta = 1.9$ ) value provides a poor fit for all the sources we singled out in earlier subsections as being potentially at higher redshifts (see Fig. 5). For local ultraluminous infrared galaxies (ULIGs), previous studies (Dunne & Eales 2001; Klaas et al. 2001) already showed this trend, with lower  $\beta$  providing a better fit when single temperature greybodies are used, whereas generally a  $\beta \sim 2$  is inferred for multitemperature fits.

Notice that in Fig. 5 we also show the 100- $\mu\text{m}$  point, although it is not included in the fits. Fitting to all four points results in poor fits either on the shorter or longer wavelength ends, depending on the choice of  $\beta$ . Presumably, to fit this wider range requires a multicomponent model, but the data do not warrant a detailed investigation of more complicated SEDs.

Thus it appears that it is reasonable to model our data as a single-temperature greybody in the limited spectral range considered (i.e. 170–850  $\mu\text{m}$ ), provided we explore the effects of varying the parameters within the accepted range we found here. Of course, this model will be incorrect in detail for the entire thermal spectrum, as has been shown previously by several authors (Stickel et al. 2000; Dunne & Eales 2001; Klaas et al. 2001; Blain et al. 2002). In gen-

**Table 3.** Fit results for all the higher- $z$  sources<sup>a</sup>.

Source	$z$	$\log(L)$ [ $L_{\odot}$ ]	$D_L$ [Mpc]
N1-078	0.66–1.00	12.1–12.6	3700–6100
N1-059	0.64–0.96	12.2–12.6	3500–5900
N1-064	0.58–0.89(0.91)	12.1–12.6	3200–5300
N1-040	0.49–0.76(0.45)	12.0–12.5	2600–4400
N1-048	0.33–0.56	11.7–12.3	1600–3000
N1-101	0.18–0.35	11.0–11.8	810–1700
N2-013	0.15–0.30	11.1–11.9	684–1500
N1-024	0.14–0.30	11.1–12.0	621–1400
N1-068	0.08–0.22(0.22)	10.4–11.5	330–1000
N1-045	0.08–0.22(0.25)	10.5–11.6	320–1000

<sup>a</sup>The ranges correspond to different  $(\beta, T_d)$  combinations – the first being (1.7, 30 K), the second being (1.5, 40 K). The redshifts in brackets are measured spectroscopically. The top half of the table has the  $>3\sigma$  detections, while the bottom half of the table has the other sources from the sample with redshifts from the fits having lower limits of greater than zero. The sources are arranged by decreasing redshift.

eral, any greybody model, even with multiple components, remains only an approximation to the underlying, far more complex dust properties. We also caution that the dust properties are merely phenomenological, corresponding to emission-weighted averages and depending on the wavelength range chosen. Care should therefore be taken in interpreting any dust temperatures physically.

### 3.6 Redshifts and luminosities

Now we wish to examine some of the physical characteristics of the non-zero-redshift sources in our sample (because they are the best constrained through their submm fluxes). Because, fundamentally, the dust spectrum/distance degeneracy is still present, derivations of properties such as luminosity have an intrinsic uncertainty. However, we can provide physical parameter estimates for what we consider to be reasonable ranges of redshifts (for the likely higher-redshift sources only) in order to obtain a handle on the physical nature of our sources, for comparison purposes.

A few of our optically fainter sources have available spectroscopic redshifts obtained from Keck and Palomar spectroscopy. These are N1-045 ( $z = 0.25$ ); N1-068 ( $z = 0.22$ ); N1-039 ( $z = 0.27$ ); N1-008 ( $z = 0.27$ ); N1-040 ( $z = 0.45$ ); and N1-064 ( $z = 0.91$ ). The details of the spectroscopic observations and the obtained redshifts are discussed elsewhere (Chapman et al., in preparation). These provide valuable checks of our redshift estimates. However, the spectroscopic redshifts only exist for a fraction of our sample, having strong selection effects. Therefore, we do not make more direct use of them, as we wish to treat our sample in a uniform way.

For definitiveness, we focus on the  $(\beta, T_d)$  combinations which agree with the SED fits (see Section 3.5), with the redshifts estimated from the submm/radio relations (Section 3.3) and with expectations from other studies (see Section 4). These are (1.7, 30 K), and (1.5, 40 K). Table 3 shows the redshift ranges, along with luminosities,<sup>4</sup> and corresponding distances for the higher-redshift candidates in our sample. The ranges illustrate how the values vary with input

<sup>4</sup>We solve for the total far-infrared luminosity by simply integrating our fitted greybody SEDs. The key mathematical step is the integral  $\int_0^{\infty} x^{s-1} (e^x - 1)^{-1} dx = \Gamma(s)\zeta(s)$ .

parameters and also give an indication of the spread of reasonable values. The sources in the upper half of the table are our  $S_{850} > 3\sigma$  detections (excluding N1-001 and N1-002, which are consistent with being at zero redshift). They are consistent with  $z \sim 0.4\text{--}0.9$  ULIGs, based on the average luminosity of this subsample being above  $10^{12} L_{\odot}$ . The likely lowest-luminosity (and redshift) source of this set is N1-048, which may be only a luminous infrared galaxy (LIG), usually defined as  $< 10^{12} L_{\odot}$ , depending on the exact dust parameters. The bottom half of Table 3 contains five LIG candidates (N1-101, N2-013, N1-024, N1-068, and N1-045), based on the range of  $(\beta, T_d)$  we considered. When comparing the redshift ranges obtained using the above rather approximate method against the known spectroscopic redshifts, we find fairly good agreement between them. This means that the assumptions made were probably reasonable. However, the two ULIGs with spectroscopic redshifts have measured values at the upper and lower end of the estimated ranges, perhaps suggesting a slightly different temperature (at least in some cases).

The only other exceptions here are N1-008 and N1-039; with their  $z_{\text{spec}} = 0.27$ , they should have been grouped with the others above. There is no reason to suspect intrinsically different dust properties in either case. It is worth noting that there are two radio sources within the N1-008 *ISO* beam. The missing submm flux of N1-039 may be related to the fact that it is one of the sources which were observed solely during the poorer weather conditions of the 2001 May observing run – rms = 2.3 mJy (see Table 1), compared to a mean rms of 1.5 mJy for the sample.

Comparing with the redshift estimates derived from the far-infrared/radio correlations (Section 3.3), we find broad agreement. The DCE relation generally gives good overlap with the other methods of estimating redshift, whereas the CY relation gives redshifts which are somewhat high. This is because the effective temperature in the DCE relation is more appropriate for our sample.

### 3.7 Star formation rates

The first star formation rate (SFR) estimator we consider is based on the far-infrared luminosities. This uses the fact that the thermal dust emission is reprocessed stellar light which was absorbed primarily in the ultraviolet (i.e. where young stars are the main contributors). For a discussion of the uncertainties associated with this and other SFR estimators, see e.g. Schaerer (1999). Essentially, the problem is to find a universal calibration, given the vastly varying conditions (e.g. different dust properties, and contribution of cirrus, stars, or AGN to the thermal spectrum) from galaxy to galaxy. Here we adopt a form which is based on stellar evolution models using a Salpeter initial mass function (Charlot et al. 2002):

$$\frac{\text{SFR}_{\text{FIR}}}{(M_{\odot} \text{ yr}^{-1})} = 1.7 \times 10^{-10} \frac{L_{\text{FIR}}}{L_{\odot}}. \quad (2)$$

The second method is based on the radio continuum, where the idea is essentially the same as above, but use is also made of the well-known far-infrared/radio correlation (see Section 3.3). Here, we use an empirical relation based on *IRAS* galaxies with radio observations (Yun, Reddy & Condon 2001):

$$\frac{\text{SFR}_{\text{rad}}}{(M_{\odot} \text{ yr}^{-1})} = (5.9 \pm 1.8) \times 10^{-22} \frac{L_{1.4\text{GHz}}}{(\text{WHz}^{-1})}. \quad (3)$$

The radio luminosity is then obtained via

$$\log L_{1.4\text{GHz}} = 20.08 + 2 \log D_L + \log S_{1.4\text{GHz}}, \quad (4)$$

where  $L$  is in  $\text{W Hz}^{-1}$ ,  $D_L$  is in Mpc and  $S_{1.4\text{GHz}}$  is in Jy.

**Table 4.** Estimating the Star Formation Rates<sup>a</sup>.

Source	$z$	$\text{SFR}_{\text{rad}} [M_{\odot} \text{ yr}^{-1}]$	$\text{SFR}_{\text{FIR}} [M_{\odot} \text{ yr}^{-1}]$
N1-078	0.66–1.00	230–640	240–730
N1-059	0.64–0.96	530–1460	250–740
N1-064	0.58–0.89	170–460	200–620
N1-040	0.49–0.76	160–450	170–580
N1-048	0.33–0.56	70–240	80–310
N1-101	0.18–0.35	20–80	20–100
N2-013	0.15–0.30	10–50	20–150
N1-024	0.14–0.30	20–110	20–160
N1-068	0.08–0.22	3–30	4–60
N1-045	0.08–0.22	3–30	5–70

<sup>a</sup>This table is arranged in an same way as Table 4.  $\text{SFR}_{\text{rad}}$  uses the relation of equation (3), whereas  $\text{SFR}_{\text{FIR}}$  uses equation (2).

We present the results in Table 4. The two estimators agree with each other reasonably well (as expected for star-forming galaxies). The strongest deviation is observed for N1-059. This source has a greater radio flux by a factor of roughly  $\sim 2$  from its peers, which may be an indication of AGN contribution. In general, estimates for lower luminosity sources are more affected by the various systematic uncertainties discussed above. The conclusions are: that the higher- $z$  candidates have  $L \sim 10^{12} L_{\odot}$  and SFRs of typically a few hundred  $M_{\odot} \text{ yr}^{-1}$ ; and that the other galaxies with estimated redshifts above 0 have  $L \sim 10^{11} L_{\odot}$  and SFRs of typically a few tens of  $M_{\odot} \text{ yr}^{-1}$ . The rest of our sample, which are more nearby, have lower  $L_{\text{FIR}}$  and SFRs, consistent with being more normal star-forming galaxies.

## 4 DISCUSSION

### 4.1 Summary of spectral properties

The multiwavelength photometric analysis of the sample of galaxies presented in the previous sections provides us with an insight into the brightest contributors to the CIB. Our sample also holds information on galaxy evolution roughly in the range  $z \sim 0\text{--}1$ .

The series of scatter plots in Fig. 3 showed that a group of five sources (N1-040, N1-048, N1-059, N1-064 and N1-078) stand out from the rest in the far-infrared/submm and submm/radio projections. Their position in the far-infrared/submm plot can be explained either by their being colder, or at somewhat higher redshift than the rest of the sample [the  $T_d/(1+z)$  degeneracy]. However, when the submm slope ( $S_{450}/S_{850}$ ) alone is examined, these sources do not stand out as one might have expected if their intrinsic SED shapes were substantially different from the rest of the sample. Thus, we assume an approximately constant SED shape across the sample, and arrive at a combined best-fitting single greybody (from the  $S_{170}/S_{450}$  and  $S_{450}/S_{850}$  slopes) with  $\beta \simeq 1.5$  and  $T_d/(1+z) \simeq 30 \text{ K}$ .

When the submm/radio relation is examined, the same group of five stands out again, with two redshift estimators agreeing with their being at higher ( $\sim 0.4\text{--}1.0$ ) redshifts. Owing to uncertainties in the spectral indices – and, more importantly, scatter in intrinsic galaxy properties – these indicators have  $\Delta z \sim 0.5$ . The DCE relation seems to provide the best fit to the available spectroscopic redshifts and may be more reliable. The above five sources are the only ones for which this relation gives a redshift of  $> 0.4$ .<sup>5</sup>

<sup>5</sup>An additional candidate is N2-013, but, on the basis of the SED fits, it appears to be a luminous infrared galaxy at perhaps up to  $z \sim 0.3$ , which is consistent with the redshifts provided by the submm/radio relations.



A different way to look at the data is to look at the submm/near-infrared relation (Fig. 4). Here, the segregation of the higher redshift candidates is most pronounced – a value of more than  $2\sigma$  separates each of the above five sources from any of the rest of the sample (although the location of N1-032 and N1-034, being faint at  $K$  and with SCUBA, is poorly understood at this point). This projection has the advantage of sampling two spectral regions with completely different emission mechanisms: thermal dust emission versus stellar light plus dust attenuation. This means that the  $T_d/(1+z)$  degeneracy is partially broken. This relation would suffer from a completely different set of systematic uncertainties than the radio/submm photometric redshifts. Such an approach was already discussed by Dannerbauer et al. (2002) in the context of their millimetre-selected galaxies compared with the *IRAS*-selected galaxies of the SLUGS sample (Dunne & Eales 2001). However, because no robust  $K$ – $S_{850}$  relation is known at present, we can do little beyond obtaining a qualitative confirmation of the relative redshifts of our sources.

Finally, we used the knowledge of the general trends in our sample, inferred from the above steps, to attempt to constrain some of the properties of the individual galaxies. We fitted single, optically thin greybodies to the 170-, 450- and 850- $\mu\text{m}$  points. For the sample as a whole, only  $\beta \simeq 1.5$ – $1.7$  provides a good fit, whereas 1.3 is a poor fit for many of the probably local sources, and 1.9 is a poor fit for our higher- $z$  candidates. Because the fits only provide  $T_d/(1+z)$ , a dust temperature needs to be assumed in order to obtain a redshift. We estimate that an acceptable range is the  $(\beta, T)$  combinations (1.7, 30 K)–(1.5, 40 K). These give redshifts which are in reasonable agreement with all relations examined so far (including the DCE and CY redshift indicators). We used this range to estimate the luminosities and SFRs of the five high- $z$  candidates, along with some intermediate sources which are possible LIGs up to  $z \sim 0.3$ , representing the tail of the more local bulk of the sample.

Our results, from near-infrared to radio, are consistent with having a sample of mostly local galaxies, some slightly higher-redshift LIGs and a handful of probable ULIGs at redshifts in the range  $0.4 < z < 1.0$ .

#### 4.2 Bimodality

Some of the scatter plots discussed above suggest a bimodality in our sample. Whether our particular observational selection effects result in bimodality in redshift, or just a higher- $z$  tail, may be an important point for distinguishing various galaxy evolution models (discussed in the next subsection). As a result of the small size of our high- $z$  candidate sample, it is difficult to test their distribution properties in detail. However, a simple test which we can perform involves comparing the  $\chi^2$  resulting from fitting a single line ( $y = mx$ ) against that for fitting two lines, both with zero  $y$ -intercept. We choose to focus on the  $S_{170}$  versus  $S_{850}$  projection, as here the bimodality is implied, but is not as clean as in the submm/near-infrared relation. We show the result in Fig. 6. We performed this test simply with the 1D  $\chi^2$  and assuming constant error for each source (because they are fairly uniformly distributed in any case). The single-line fit results in a  $\chi^2$  of 108, whereas the two-line fit results in a  $\chi^2$  of 37, with  $N = 31$  (minus either one or two constraints); for the two-line fit, we use the nearest line for each point. The two-line model thus provides an adequate fit to the data, suggesting that each source is drawn from either one population or the other. This supports the idea that a handful of our sources are a distinct population and lie at  $z \sim 0.4$ – $0.9$ , whereas most of the sample are at  $z \sim 0$ .

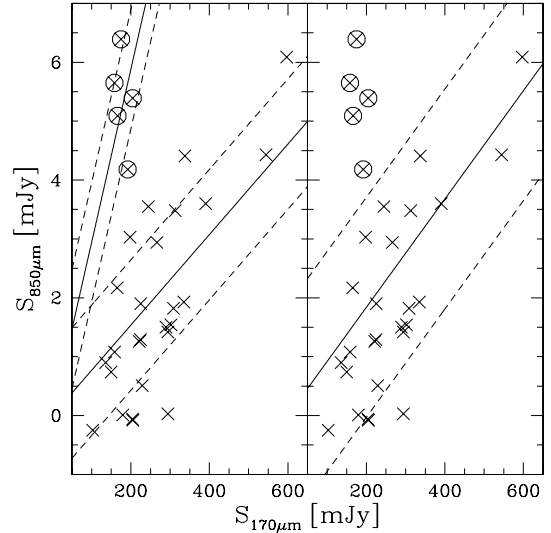


**Figure 6.** Here we test the hypothesis of our sample being bimodal by comparing the  $\chi^2$  of a single-line fit for the entire sample (right-hand panel) with a two-line fit for each subsample (left-hand panel). The dashed lines are  $\pm 1\sigma$ , where  $\sigma$  is the rms scatter in the  $y$ -direction. Notice that, apart from N1-048, even with the single-line fit to the entire sample, our high- $z$  candidates are  $>2\sigma$  away from the best-fit line. See Fig. 3 for representative error bars.

#### 4.3 Comparison with evolutionary models

The sources studied here are a representative sample of the brightest  $\sim 10$  per cent of sources contributing to the CIB. They thus provide a test of the various evolutionary models abounding in the literature. Models which are consistent with both the observed CIB intensities, and the number counts obtained by various surveys, imply that the majority ( $\sim 80$  per cent) of the CIB near its peak ( $\sim 200 \mu\text{m}$ ) will be resolved by sources in the range  $0 < z < 1.5$ . The same redshift range sources contribute only  $\sim 30$  per cent of the 850- $\mu\text{m}$  background (Chary & Elbaz 2001; Elbaz et al. 2002). Such models result in a peak of the SFR density at  $z \sim 1.0$  and then have their SFR essentially flat until  $z \sim 4$ . In general,  $>70$  per cent of the star formation takes place in galaxies with  $L_{\text{FIR}} > 10^{11} L_{\odot}$  (Chary & Elbaz 2001).

From the redshifts we infer for our sample, our sample seems to span the crucial epoch over which the strongest evolution of the SFR density takes place. In general, there is no way to fit the FIRBACK counts without strong far-infrared evolution over at least this redshift range. Adopting the starburst template from Lagache, Dole & Puget (2002), we see that sources less luminous than about  $10^{12} L_{\odot}$  fall below the FIRBACK detectability beyond a redshift of  $\sim 0.4$ . Because the FIRBACK selection excludes normal galaxies beyond  $z \sim 0.1$  and LIGs beyond  $z \sim 0.3$ , but allows for higher-luminosity sources up to  $z \sim 1.0$ , our mix of normal, star-forming galaxies, including a few possible LIGs and a handful of most likely higher- $z$  ULIGs, is in good qualitative agreement with this model. The bimodality which this hints at for our selection (and which we appear to observe), is more directly shown by a number of specific models (Dole et al. 1999; Wang & Biermann 2000; Chary & Elbaz 2001; Franceschini et al. 2001; Chapman et al. 2002; Lagache et al. 2002). An easy way to achieve such a bimodal distribution is to phenomenologically decompose the luminosity function into a component of normal, quiescent galaxies and a much more luminous component of

ULIGs, and then have the luminous component evolve more strongly than the quiescent one so that it dominates the luminosity function by  $z \sim 1$  (Dole et al. 1999; Wang & Biermann 2000; Franceschini et al. 2001). This approach was exploited in the context of the FIRBACK sources (Lagache et al. 2002), showing that a double-peaked redshift distribution is predicted, as appears to be confirmed by our data.

Another approach to modelling the  $N(z)$  distribution is that of Chapman et al. (2002), where the entire infrared luminosity function is evolved. This combines the colour (i.e. temperature) distribution of local galaxies with a strong luminosity evolution, such as in Xu (2000), to produce the  $N(z)$  distribution for the FIRBACK population. A bimodality can only be produced here if a bivariate  $T_d$  distribution is used (i.e. by including cold luminous sources), but this is strongly evolution dependent. Discriminating in detail between such models, including issues such as separating density evolution from luminosity evolution, is not currently possible. However, once the full redshift distribution of the FIRBACK sample is obtained, such discrimination may be feasible.

The FIRBACK selection allows us to investigate the range  $0 \lesssim z \lesssim 1$ . On the other hand,  $z \sim 1$  is the lower limit of submm/millimetre selected surveys (Smail et al. 2002; Dannerbauer et al. 2002). Thus samples such as ours should act as a bridge between the local Universe and the much higher redshift population detected in long-wavelength surveys. We illustrated this explicitly in Fig. 4, where we overlaid a number of SCUBA-selected sources and showed that they occupy essentially the same submm/near-infrared locus as our high- $z$  candidates.

#### 4.4 Conclusions

We have learned that the brightest  $\sim 10$  per cent of the CIB is composed of two different types of galaxy: about one-sixth are the low redshift tail of a rapidly evolving ULIG population (similar to the higher- $z$  SCUBA sources); and the other five-sixths are mainly nearby quiescently star-forming galaxies like the Milky Way, with perhaps a few more luminous infra-red galaxies in between. This is somewhat contrary to early expectations for the nature of the FIRBACK galaxies (e.g. Puget et al. 1999), where some sources in the range  $z \sim 1 - 2$  were expected. This would be the appropriate range for the handful of higher- $z$  sources in our sample only if a much warmer SED is assumed. However, this is inconsistent with the redshift and temperature estimates for the majority of our sample, ruling out such models. Further progress on constraining models in detail will come from spectroscopic and morphological studies of the entire sample. Understanding what makes up the other  $\sim 90$  per cent of the CIB will need to await future far-infrared missions with smaller beam sizes, such as the *Balloon-borne Large Aperture Sub-millimetre Telescope (BLAST)* and *Herschel*, as well as high sensitivity mid-IR facilities such as the *Space Infrared Telescope Facility (SIRTF)*.

#### ACKNOWLEDGMENTS

We thank the staff of the JCMT for their assistance during the observations. This research was supported by the National Research Council (NRC) and by the Natural Sciences and Engineering Research Council of Canada. HD acknowledges funding from the MIPS project, which is supported by NASA through the Jet Propulsion Laboratory, subcontract #P435236. The James Clerk Maxwell Telescope is operated by the Joint Astronomy Centre on behalf of the Particle Physics and Astronomy Research Council of the United

Kingdom, the Netherlands Organization for Scientific Research, and the National Research Council of Canada. This research has made use of the NASA/IPAC Extragalactic Database (NED) which is operated by the Jet Propulsion Laboratory, California Institute of Technology, under contract with the National Aeronautics and Space Administration.

#### REFERENCES

- Archibald E., Wagg J. W., Jenness T., 2000, JAC, JCMT, <http://www.jach.hawaii.edu/JACdocs/JCMT/SCD/SN/002.2/>
- Barger A. J., Cowie L. L., Sanders D. B., 1999, AJ, 518, L5
- Bell E. F., 2003, ApJ, 586, 794
- Blain A. W., Kneib J. -P., Ivison R. J., Smail I., 1999, ApJ, 512, L87
- Blain A. W., Smail I., Ivison R. J., Kneib J.-P., Frayer D. T., 2002, Phys. Rep., 369, 111
- Bridger A. et al., 2000, SPIE, 2009, 227
- Carilli C. L., Yun M. S., 2000, ApJ, 530, 618
- Chapman S. C., Lewis G., Scott D., Borys C., Richards E., 2002, ApJ, 570, 557
- Chapman S. C., Smail I., Ivison R. J., Helou G., Dale D. A., Lagache G., 2002, ApJ, 573, 66
- Charbonneau P., 1995, ApJ, 101, 309
- Charlot S., Kauffmann G., Longhetti M., Tresse L., White S. D. M., Maddox S. J., Fall S. M., 2002, MNRAS, 330, 876
- Chary R., Elbaz D., 2001, ApJ, 556, 562
- Ciliegi P. et al., 1999, MNRAS, 302, 222
- Cowie L. L., Barger A. J., Kneib J.-P., 2002, AJ, 123, 2197
- Dannerbauer H., Lehnert M. D., Lutz D., Tacconi L., Bertoldi F., Carilli C., Genzel R., Menten K., 2002, ApJ, 573, 473
- Davis R., Burston A., Ward M., 2002, MNRAS, 329, 367
- Dole H. et al., 2000, in Lemke D., Stickel M., Wilke K., Lect. Notes Phys. Vol. 548, *ISO surveys a dusty Universe*. Springer, Ringberg, p. 54
- Dole H. et al., 2001, A&A, 372, 364
- Dunne L., Eales S. A., 2001, MNRAS, 327, 697
- Dunne L., Clements D. L., Eales S. A., 2000, MNRAS, 319, 813
- Dwek E. et al., 1998, ApJ, 508, 106
- Elbaz D. et al., 1999, A&A, 351, L37
- Elbaz D., Cesarsky C. J., Chaniol P., Aussel H., Franceschini A., Fadda D., 2002, A&A, 384, 848
- Fabian A. C. et al., 2000, MNRAS, 315, 8
- Fadda D., Flores H., Hasinger G., Franceschini A., Altieri B., Cesarsky C. J., Elbaz D., Ferrando Ph., 2002, A&A, 383, 838
- Fixsen D. L., Dwek E., Mather J. C., Bennett C. L., Shafer R. A., 1998, ApJ, 508, 123
- Finkbeiner D. P., Davis M., Schlegel D. J., 2000, ApJ, 524, 867
- Franceschini A., Aussel H., Cesarsky C. J., Elbaz D., Fadda D., 2001, A&A, 378, 1
- Gautier C., III, Boulanger F., Perault M., Puget J. L., 1992, AJ, 103, 1313
- Hauser M. G., Arendt R. G., Kelsall T. et al., 1998, ApJ, 508, 25
- Helou G., Beichman C. A., 1990, in Kaldeich B., ed., Proc. 29th Liege Int. Astrophys. Colloq., From Ground-Based to Space-Borne Sub-mm Astronomy. ESA SP-314, 117
- Holland W. et al., 1999, MNRAS, 303, 659
- Hornschemeier A. E. et al., 2000, HEAD (High Energy Astrophysics Division of the AAS), 32, 2613
- Ivison R. J. et al., 2002, MNRAS, 337, 1
- Jenness T., Lightfoot J. F., 1998, in Albrecht R., Hook R. N., Bushouse H. A., eds, ASP Conf. Ser. Vol. 145, *Astronomical Data Analysis Systems and Software*. Astron. Soc. Pac., San Francisco, p. 216
- Juvela M., Mattila K., Lemke D., 2000, A&A, 360, 813
- Kakazu Y. et al., 2002, (astro-ph/0201326)
- Klaas U. et al., 2001, A&A, 379, 823
- Lagache G., Puget J.-L., 2000, A&A, 355, 17
- Lagache G., Abergel A., Boulanger F., Désert F. X., Puget J.-L., 1999, A&A, 344, 322

- Lagache G., Haffner L. M., Reynolds R. J., Tufte S. L., 2000, *A&A*, 354, L247
- Lagache G., Dole H., Puget J.-L., 2002, *MNRAS*, 338, 555
- Lilly S., Eales S. A., Gear W. K., Webb T. M., Bond J. R., Dunne L., 1999, in Carollo C. M., Ferguson H. C., Wyse R. F. G., eds, *The formation of galactic bulges*. Cambridge Univ. Press, Cambridge, p. 26
- Magliocchetti M., Maddox S. J., Wall J. V., Ben C. R., Cotter G., 2000, *MNRAS*, 318, 1047
- Puget J.-L., Abergel A., Bernard J. P., Boulanger F., Burton W. B., Désert F. X., Hartmann D., 1996, *A&A*, 308, L5
- Puget J.-L. et al., 1999, *A&A*, 345, 29
- Saunders D. B., Mirabel I. F., 1996, *ARA&A*, 34, 749
- Schaerer D., 1999, in Hammer F., Thuan T. X., Cayette V., Guiderdoni B., Van J. T. T., eds, *Building galaxies*, p. 389
- Scott D. et al., 2000, *A&A*, 357, L5
- Smail I., Ivison R. J., Blain A. W., Kneib J.-P., 2002, (astro-ph/0112100)
- Soifer B. T., Sanders D. B., Madore B. F., Neugebauer G., Danielson G. E., Elias J. H., Lonsdale C. J., Rice W. L., 1987, *ApJ*, 320, 238
- Stickel M. et al., 2000, *A&A*, 359, 865
- Wang Y., Biermann P. L., 2000, *A&A*, 356, 808
- Willott C. J., Rawlings S., Jarvis M. J., Blundell K. M., 2003, *MNRAS*, 339, 173
- Xu C., 2000, *ApJ*, 541, 134
- Yun M. S., Reddy N. A., Condon J. J., 2001, *ApJ*, 554, 803

This paper has been typeset from a  $\text{\TeX}/\text{\LaTeX}$  file prepared by the author.